Eng. Sci., 2025, **37**, 1767

Engineered Science
DOI: https://dx.doi.org/10.30919/es1767

A Tantalum Wire-Reinforced Porous Magnesium Scaffold for Bone Repair

Dong Wang,[1,*] Jun Li,[1] Yonggang Guo,[1] Lan Wu,[1] Yong Chang,[1,*] Ze Chai[2,*] and Xianlong Zhang[3]

Abstract

Porous magnesium (P-Mg) is widely applied as an implant material in bone repair, and in clinical application its mechanical and biological properties are the focus of concern. In this work, a porous magnesium reinforced by tantalum wires (P-MT) was successfully fabricated via the infiltration casting technology, and the relevant mechanical and biological properties were systematacially investigated. The prepared P-MT was composed of Mg matrix, uniformly embedded tantalum (Ta) wires, and isodiametric, interconnected holes. Both the compressive yield strength and elastic modulus of the P-MT were remarkably higher than those of the conventional P-Mg, owing to the deformation-resistance enhancement and supporting effect from the hard Ta wires within the former configuration. With increasing the porosity of the P-MT from 30% to 50%, the yield strength gradually decreased from 20.2 MPa to 10.8 MPa and likewise the elastic modulus from 3.5 GPa to 1.5 GPa. In Hank's solution, the P-MT exhibited an initially high and subsequently low degradation rate compared with of the P-Mg. *In vivo* evaluations revealed that the introduced Ta wires can provide stable attachment sites for new bones ingrowth into the P-MT scaffolds, thereby gaining superior osseointegration. The P-MT material has a promising application in bone repair engineering.

Keywords: Porous material; Infiltration casting; Microstructure; Mechanical properties; Osseointegration.
Received: 17 July 2025; Revised: 16 September 2025; Accepted: 21 September 2025
Article Type: Research article.

1. Introduction

Magnesium (Mg) and its alloys are nowadays widely used as implant materials in bone repair and regeneration due to their distinct characteristics, such as good biocompatibility, low-priced, degradability and low density (Fig. 1a).[1,2] However, the dense Mg (D-Mg) was not beneficial to the new bone ingrowth into the implants, and might cause failure of the bone-implant interface during implantation.[3] To improve the osteoconduction of the Mg implants, a porous structure is usually necessary, which could effectively accelerate the body fluid transmission into the implants, thereby promoting the new bone formation.[4]

So far, various techniques have been developed to fabricate porous Mg (P-Mg) scaffolds, such as hydrogen injection,[5] salt pattern molding,[6] powder metallurgy,[7] 3D rapid printing,[8] etc. The P-Mg with unidirectional pores prepared by hydrogen injection[5] reportedly had a good biocompatibility and suitable corrosion rate. Seyedraoufi *et al.*[7] developed the P-Mg with an open-pore structure by powder metallurgy. When having the porosity of 21%-36%, the P-Mg exhibited a satisfied mechanical property that was comparable to the cancellous bone. Yue *et al.*[8] prepared the P-Mg with a uniform pore structure by 3D printing, and the relevant porosity, pore shape and size could be accurately controlled. Recently, a novel preparation technology, *i.e.*, the infiltration casting followed by selectively dissolving the precursors, was developed to fabricate the P-Mg scaffolds.[9,10] The as-prepared P-Mg exhibited an interconnected, controllable and open pore structure, which was efficient in improving the osseointegration of the implants.[11] It was worth noting that the mechanical property of the P-Mg would decay in the body fluids because of the inevitable degradation of Mg matrix.[12] A poor mechanical property always led to the premature failure of orthopedic implants.[13] Therefore, the mechanical property of the P-Mg was one of focal points in the application of orthopedic implants.

The mechanical property of P-Mg implants depended mainly on the pore structure and metal or alloy itself.[14-16] Zou *et al.* investigated the influence of porosity on compressive property of P-Mg scaffolds.[14] The result indicated that the compressive yield strength of P-Mg decreased from 16.2 MPa

---

[1] *Henan Key Laboratory of Superhard Abrasives and Grinding Equipment & School of Mechanical and Electrical Engineering, Henan University of Technology, Zhengzhou, 450001, China*
[2] *School of Aerospace Engineering and Applied Mechanics, Tongji University, Shanghai, 200092, China*

to 0.7 MPa with increasing the porosity from 28.4% to 62.4%. It was also reported that the carbon nanotubes could be doped into the P-Mg by powder metallurgy.[15] Though the improved mechanical property of the doped P-Mg scaffolds, the biocompatibility of the carbon nanotube additives remained unknow. Lee *et al.* investigated the influence of Ag addition on the mechanical property of P-Mg, suggesting that a 3 wt%-Ag addition resulted in an approximately 20% increase in the compressive strength of P-Mg.[16] It was worth noting that the metal Ag could accelerate the corrosion rate of the P-Mg, due to the significantly increased number of active sites for corrosion attack. Rajan *et al.* assessed the degradation behavior of Mg alloys coated by tantalum (Ta), and found that Ta coating significantly enhanced the corrosion resistance of Mg alloys.[17] Besides, Ta basically has higher mechanical strength and modulus than Mg.[18,19] Unfortunately, the refractory Ta could not be directly added into Mg due to the inferior intermiscibility of the two metals.[20] In this work, Ta wires would be implanted into Mg ingots, and expectantly serve as reinforcers to improve the mechanical property of P-Mg scaffolds.

On the other hand, the satistactory repair of bone defects commonly required good osseointegration of implants.[21] The influence of the porosity on bone regeneration of P-Mg scaffolds via in vivo experiments was investigated.[22] The result showed that the area of newly formed bone area in the scaffolds gradually increased as the porosity increased from 24% to 40%. However, a high porosity often led to excessively quick degradation and inferior mechanical property of the P-Mg scaffolds.[23,24] Surface modification was an effective method to enhance the osseointegration of P-Mg scaffolds. For instance, the scaffold coated by Ta exhibited well cell viability and osseointegration.[17] Nevertheless, the immersion-prepared Ta coating always possessed a poor homogeneity in the thickness, which most likely deteriorated the osseointegration of P-Mg scaffolds. As a cortical bone substitute, porous Ta scaffolds could be directly implanted into the femurs of rabbits.[25] It has demonstrated that within the porous Ta the new bone volume was greater than that within the porous Ti6Al4V after implantation of both 4 and 8 weeks, indicating better osteointegration of the porous Ta.

In this study, the P-Mg reinforced by Ta wires (P-MT) was fabricated by the infiltration casting and followed by selective corrosion technology. The compressive properties including elastic modulus and yield strength and degradation behavior of the P-MT scaffolds were investigated. Besides, the relevant biological performance, *i.e.*, cytotoxicity, cell viability, cell differentiation, and osseointegration, were comprehensively investigated by in vitro and in vivo experiments. With the help of finite element software, the mechanism underlying the Ta wire-induced strengthening of P-MT scaffolds was revealed. The influencing mechanism of the Ta wires on the osseointegration of the P-MT scaffolds was clarified. Compared with the P-Mg scaffold, the P-MT one displayed excellent mechanical properties and superior osseointegration, and it has great application potential in bone defect repair.

2. Materials and methods

2.1 Material fabrication

Commercial-purity Mg (purity: 99.6%, Baowu Magnesium Technology Co., Ltd., CHN) was used as the matrix constituent, which had a compressive yield strength of 53 MPa and modulus of 42 GPa.[9] The as-annealed titanium (Ti) wires (purity: 99.9%, Shanxi Super Co., Baoji, China) with 0.40 mm diameter were utilized as the space holder. The Ta wires (purity: 99.9%, Shanxi Super Co., Baoji, China) with a diameter of 0.15 mm was regarded as the reinforced fibers. The compressive yield strength and elastic modulus of the metallic Ta were approximately 286 MPa and 185 GPa, respectively.[18,26] The infiltration casting technology was employed to prepare the P-MT material. As illustrated in Fig. 1b, the preparation process of the P-MT involved the following key steps: (1) the intertwined Ti/Ta composite wires were weaved into a pre-designed 3D porous structure, in which the length radio of the Ti to Ta wires was 1:2, (2) the Mg ingot was heated to 700 °C under argon gas, infiltrated into the 3D porous structure with pressure of 0.2 MPa to form a Mg/Ti/Ta composite, and then rapidly transferred to cold water, and (3) the Ti wire was selectively removed by 3.0 M hydrofluoric acid (HF) solution at ambient temperature, leaving the Ta-implanted P-MT. Both the bubble method and the weight method were used to examine the termination of the chemical reaction.[27] Moreover, the P-Mg as the control group was also prepared by the infiltration casting technology.[9]

The porosity was tailored by changing the volume fraction of the space holder in the green composite. The porosities of P-MT-30%, P-MT-40%, P-MT-50%, and P-Mg-50% specimens were controlled to be 30.0 ± 2.0 %, 40.0 ± 2.0 %, 50.0 ± 2.0 % and 50.0 ± 2.0 %, respectively. The pore diameter of the P-MT material was identical to the diameter of the space holder. The as-prepared P-MT material was machined into cylinders with size of Φ 10.0 mm × 10.0 mm for compressive tests, slices with size of Φ 2.0 mm × 10.0 mm for in vitro experiments, and cylinders with size of Φ 3.0 mm × 6.0 mm for in vivo experiments.

2.2 Materials characterization

---

[3]*Department of Orthopaedics, Shanghai Jiao Tong University Affiliated Sixth People's Hospital, Shanghai, 200233, China*
[*]*Email:* zzwd2019@haut.edu.cn (Dong Wang), changyong@haut.edu.cn (Yong Chang), chaize@sinap.ac.cn (Ze Chai)

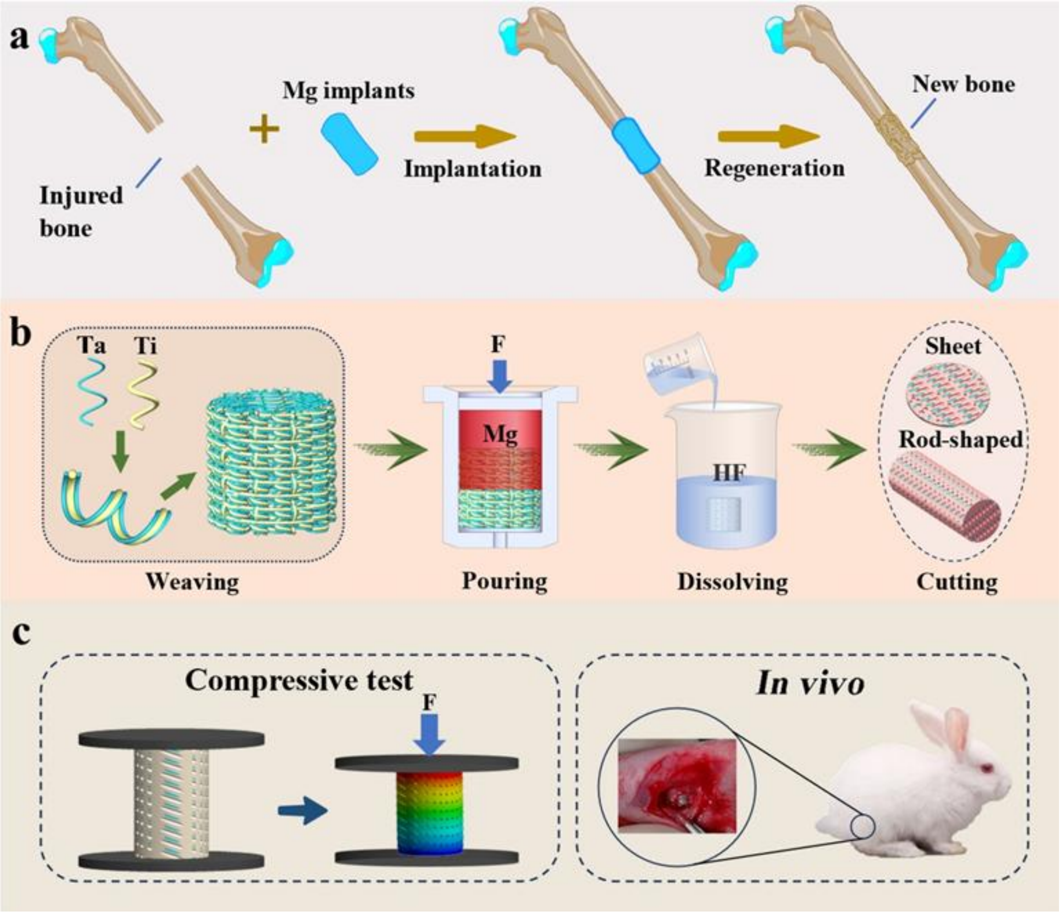

Fig. 1: (a) The repairing process of bone defects with Mg implants, (b) Schematic diagram of the preparation process of the P-MT material, (c) Evaluation of compressive properties and osseointegration of the P-MT material.

The macro morphology of the scaffolds was examined by a digital camera (Olympus: E-M10, JPN). The relevant structure was observed by using an optical microscope (DSX100, JPN) and a field emission scanning electron microscope (SEM, JSM7600F, JPN) and an energy dispersive X-ray spectroscopy detector (EDS). In addition, the relevant phases were determined via an X-ray diffractometer (XRD, Miniflex600, JPN) with a 2θ range of 20-80° at 2°/min scanning rate.

The compressive tests were carried out by using the CMT 5105 testing machine according to ASTM: E9-09 at 0.5 mm/min strain rate and room temperature (Fig. 1c). The compressive yield strength of the specimens was directly obtained from the 'yield point' at which the material densification started.[28] The elastic modulus of the compression specimens was determined from the gradient of the linear elastic stage. The experimental error was minimized by applying the machine compliance corrections.[29] For each group, at least three specimens were repeatedly tested to ensure the high accuracy of the data.

2.3 Degradation test

The degradation tests of P-MT specimens, with porosity of 30 % and size of 10.0 mm × 10.0 mm × 3.5 mm, were performed in Hank's solution at 37 ± 1.0 °C. The P-Mg specimens with the same size and porosity were served as a control group. The immersion time of the specimens was set as 0 - 192 h with a 16 h-test interval. After each immersion, the degradation products on the specimens were removed by ultrasonic method. The macro morphology of the degraded specimens was characterized by the Olympus camera. The pH values of the residual solutions were determined by a pH analyzer (PHS-3CW, CHN). The evolved hydrogen was directly measured from an upper burette. An average value was calculated from three measurements.

2.4 Finite element analysis

A finite element software (Abaqus 6.14) was employed to stimulate the biomechanical distribution and deformation of the specimens. Both P-MT and P-Mg computed models with 30% porosity and 2.0 mm pore size were established, respectively. Besides, P-Mg reinforced by discontinuous Ta stick (P-MDT) model with the same porosity and pore size was also established. The diameter of Ta wires in the models was 1.0 mm. The length of Ta sticks in the P-MDT model was

1.5 mm. The dimension of the cylindrical model was Φ 40 mm × 10 mm. The mesh shape of the model was regular tetrahedron, and the edge length was 0.2 mm. The elastic moduli of Mg and Ta were set as 42 GPa and 185 GPa, respectively, and the corresponding Poisson's ratios were 0.33 and 0.35, respectively. The loading rate of the models was 0.5 mm/min. A bonded contact was established between the Ta wire and the Mg matrix to streamline the simulation process.

2.5 Cell responses in vitro

2.5.1 Cell culture

The MG63 osteoblasts were used to evaluate the biocompatibility of the as-fabricated scaffolds. The osteoblasts were cultivated in the mixture medium of Dulbecco's modified Eagle's medium (DMEM, 100 μg/ml, Gibco) and 10% fetal calf serum (Gibco) under a humid atmosphere of 5% CO2 at 37°C. After sterilization, the cages were instantly transferred into 24-well plates (1 × 104 cells per well) for the cell cytotoxicity, proliferation and differentiation.

2.5.2 Indirect cytotoxicity and proliferation

The scaffolds were immersed in the mixture of DMEM and 10% fetal calf serum for 24 h under the humid of 5% CO_2 and 37 °C. The extract was gained at a ratio of 3.0 cm^2/ml. Afterwards, the immersion solution was centrifuged. Finally, the supernatant was collected without any filtration.

After incubating for 24 h, the morphologies of the osteoblasts adhered on the scaffolds were observed. The cells were firstly fixed with 4.0% paraformaldehyde for 20 min, permeabilized using 0.1% Triton X-100, and then blocked by 10% goat serum for another 20 min. The cells were cultured by rhodamine-phalloidin (1:40 diluted blocking buffer) for 1 h at 37 °C. Cytoskeleton was stained with FITC-Phalloidin when nuclei were counterstained by fluorescent dye DAPI (4, 6-Diamidino-2-phenylindole). The cell morphology was examined by a fluorescence microscope (Leica DM400, DE). The cytotoxicity of the extracts at a concentration of 100% was evaluated using Live/Dead assays. MG63 cells were cultivated in the 24-well plates for 1and 3 days, respectively. After incubation, all the plates were carefully washed by Phosphate-Buffered Saline (PBS) solution containing 50 μg/ml of propidium iodide. Additionally, each well was injected with 200 μl of fresh solution of fluorescein diacetate consisting of D-PBS and EthD-1. MG63 cells were then cultured under a humid atmosphere for 5 min. Next, the status of the cells was assessed by a Live/Dead Kit stain (Invitrogen, Carlsbad, CA). The cells were examined under an upright red and green light fluorescence microscope (Leica DM400, DE).

MTT assay was implemented to quantitatively assess cell viability at every time nodes. The culture medium without the scaffold extracts was regarded as negative control group. The blank plate was served as blank control group. After 24 h incubation, the culture medium was substituted with the extracted medium. The samples were further incubated for 1, 3 and 7 days, respectively. MTT solution of 10 μl (1 mg/mL diluted culture media) was injected to each well for 2 h. Besides, the 100 μl solution containing 10% sodium dodecyl sulfate and 0.01 M hydrochloric acid was injected to wells in the dark. Finally, the absorbance of the wells was tested by using a spectrophotometer (Bio-Rad, USA) at a wavelength of 450 nm. The cell viability was evaluated according to the previous report.[11]

2.5.3 Alkaline phosphatase activity

MG-63 osteoblasts with a density of 1 × 10^4 cells/well were seeded into the 24-well plates and cultivated in the medium for 1 day. After the culture medium was replaced with the scaffold extracts, the cells continued to be incubated for 7 days and 14 days. Afterwards, the cells in the wells were cleaned three times with the PBS. After the supernatants were aspirated, the washed cells were incubated with 50 μl of Alkaline phosphatase activity (ALP) buffer solution consisting of assay buffer dissolved by two tablets p-nitrophenyl phosphate (pNPP) (Sigma). After a period of 60 min, ALP activity of the cells was acquired at 405 nm with the acid of an enzyme-linked immunosorbent assay (ELISA, Thermo, USA).

2.6 Osseointegration in vivo

2.6.1 Surgical procedures

The animal experiment protocol was first approved by the Animal Care and Use Committee of Shanghai Jiao Tong University Affiliated Sixth People's Hospital. Animal management procedures were implemented under the guide of the Animal Care and Use Committee. Adult New Zealand White (NZW) rabbits (male or female) with wights of 2.5-3.0 kg were applied to investigate the osseointegration of the P-MT scaffolds on long-bone segmental defects. Eight rabbits were equally divided into two groups, *i.e*. P-MT group and P-Mg group. The surgery was implemented to remove a part of the femurs (Φ 3 mm × 6 mm) after the rabbits were fed for a week. The P-MT scaffolds with an identical size were implanted into the defects. The surgical wound was carefully sutured. The new bone formation was evaluated by a polychrome fluorescent labeling method. After the surgery of 6 and 12 weeks, calcein (20 mg/kg) was directly injected to identify the newly formed bone. The calcein labeling area fraction in the defects was calculated by an Image

Pro Plus software.

2.6.2 Micro-computed-tomography examination

After implantation of 8 and 16 weeks, all the rabbits were euthanized to harvest the complete femurs. The scaffolds were fixed with paraformaldehyde for 1 day. Micro-computed-tomography (Micro-CT, PerkinElmer, USA) was used to evaluate the bone regeneration of the scaffolds.[30] The 2D images of the scaffolds were rebuilt by the NRecon (Skyscan, DE). Meanwhile, 3D model of the new bone was generated by CTVol (Skyscan, DE). Both the bone mineral density (BMD) and the bone volume fraction (bone volume in total scaffold volume, BV/TV) were measured at post-implantation of 8 and 16 weeks.

2.6.3 Histological analysis

The femur condyles were fixed in 10 % v/v formalin solution for 2 days, decalcified with 10% v/v EDTA (pH 7.4) for 14 days, and then embedded in polymethyl methacrylate (DASF, Germany). For each scaffold, transverse sections were cut by a tissue microtome (SP1600, Leica, DE), and polished to a thickness of 50 μm. The fluorochrome markers in the scaffolds were examined by a confocal laser-scanning microscopy (CLSM, Leica, DE). The thin slices were stained by 1% acid fuchsin and 1.2% trinitrophenol. The histological images were acquired by using an optical microscope (LeicaDM400, DE).

2.7 Statistical analyses

In vitro and in vivo femur experiments in this work were carried out at three times. The data results were available for analysis in the form of the mean value ± standard deviation (SD) at each group. A statistical significance was evaluated by a standard one-way ANOVA. $p < 0.05$ was defined to be statistically significant.

3. Results

3.1 Microstructure characterization

Fig. 2 exhibits the macroscopic appearance of the P-MT specimen prepared via the infiltration casting technology. The cylindrical P-MT specimen was cut longitudinally. As shown in Fig. 2a, the cross section was composed of Mg matrix, holes and Ta wires. The diameters of the holes and Ta wires were 0.40 mm and 0.15 mm, respectively. Both the holes and the Ta wires were uniformly distributed in the Mg matrix. A lot of holes with the same diameter, formed after removal of the Ti wires, were inter-connected, which would be beneficial to the transportation of the body fluids in the P-MT specimen. There were no other structural defects on the Mg matrix except for these holes. The outer surface of the cylindrical specimen had similar appearance, as seen in Fig. 2b. As shown in Fig. 2c, the square zone on the section was magnified to examine the shape of the Ta wires and holes. Both the wires and holes on the section were irregular, *e.g.* circular, elliptical and tunnel-like. A SEM micrograph in Fig. 2d displays the interface between the Ta wires and Mg matrix, where the wires were well-embedded in the matrix, and no pores or impurities could be found. EDS line scanning was carried out across the Ta wires in the Mg matrix. As shown in Fig. 2d, the Ta and Mg elements exhibited significant fluctuations at the Ta/Mg interface, indicating that Ta was not melted in the Mg matrix during infiltration casting. The diameter of the embedded wire was 150 μm, identical to that of the as-prepared states, further suggesting that during casting the Ta wires were not dissolved. Fig. 2e shows an amplified SEM micrograph of the holes on the section. The tunnel-like channel was formed after the Ti wires were dissolved in the hydrofluoric acid solution. The flow line reliefs, arranged parallel to the axis of the channel, could be observed on the inner surface of the channel. Only a single MgF_2 layer was formed on the channel surface (zone "P" in Fig. 2e), as indicated in Fig. 2h. Fig. 2f presents the XRD pattern of Mg/Ti/Ta composite, where the α-Mg (JCPDS 35 – 0821) matrix, Ti (JCPDS 44 – 1294) and Ta (JCPDS 04 – 0788) metals were detected. As the Ti wires were removed, the P-MT specimen was comprised of only two phases, α-Mg and Ta, as seen in Fig. 2g.

3.2 Mechanical property and degradation behavior

Fig. 3a shows the P-MT specimens with different porosities. The number of holes in the specimens decreased as the porosity decreased from 50% to 30%. According to the length and diameter ratios of Ti to Ta wires, the volume fraction of Ta in the composite increased from 12.0% to 28.0% with increasing the porosity from 30% to 50%. The cell wall thickness (CWT) of the specimens was calculated by Image Pro Plus software. As shown in Fig. 3b, the CWT values of the P-MT specimens mainly lay in the range of 0 - 400 μm. The average CWT value of the P-MT specimens increased from 241.4 μm to 308.2 μm as the porosity decreased from 50% to 30%. The stress-strain curves of the specimens were obtained from the compressive tests. As seen in Fig. 3c, the stress-strain curves could be basically divided into three regions, *i.e.*, a linear elastic, a pseudo-plateau stress and a densification region. At the porosity of 50%, the elastic modulus and the yield strength of the P-MT specimens were 1.5 GPa and 10.8 MPa, while for the P-Mg specimens, they were 0.8 GPa and 5.6 MPa, respectively. Obviously, the elastic modulus and the yield strength of the P-MT specimens were higher than those of the P-Mg specimens. Note that the porosity also played a

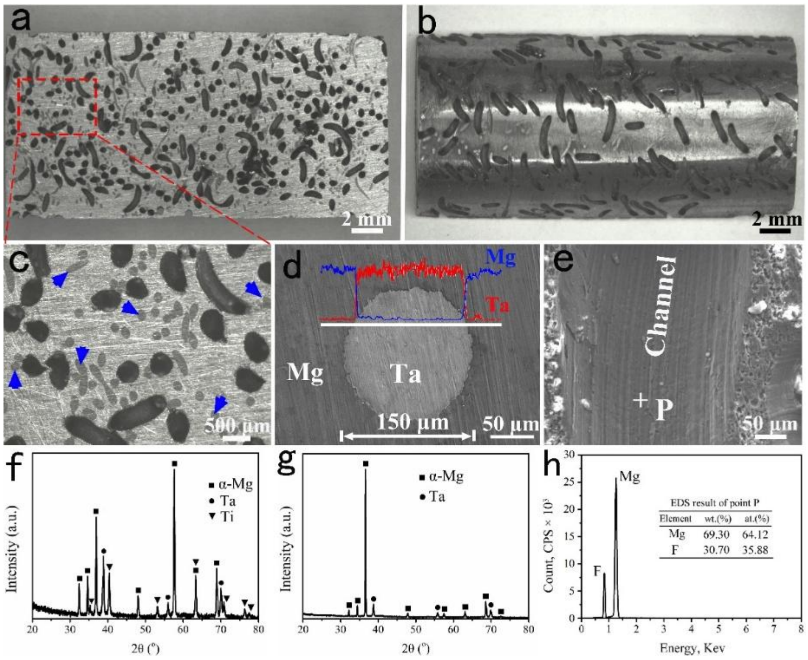

Fig. 2: Macroscopic appearance of the P-MT specimen along the axial direction. (a) Cross section, (b) Outer surface, (c) Enlarging image of square zone as marked on (a), Blue arrows pointed the positions of the Ta wires embedded in Mg matrix, (d) SEM micrograph of the Ta wires embedded in Mg matrix, (e) SEM micrograph of channels on the section, (f) XRD pattern taken from the Mg/Ti/Ta composite, (g) XRD pattern taken from the P-MT specimen, (h) EDS profile of P point on the inner surface of channel pores in Fig. 2e.

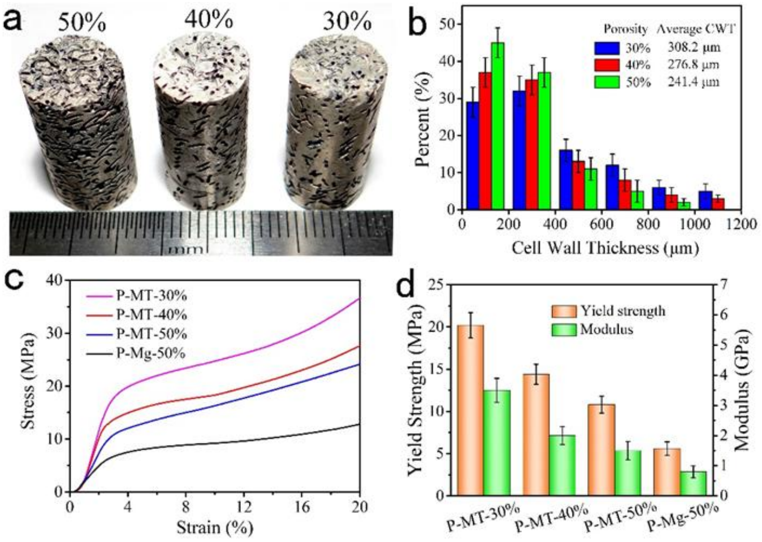

Fig. 3: (a) Macroscopic appearance of the P-MT specimens with different porosities, (b) The size distribution of the average cell wall thickness (CWT) of the P-MT specimens with different porosities, (c) Nominal compressive stress-strain curves of the P-MT and P-Mg specimens during quasi-static compression, (d) The compressive yield strength and elastic modulus of the different specimens.

significant role on the compressive properties of the specimens. As the porosity decreased from 50% to 30%, the elastic modulus increased from 1.5 GPa to 3.5 GPa, and accordingly the compressive yield strength of the P-MT increased from 10.8 MPa to 20.2 MPa (Fig. 3d).

The structure models of specimens including P-MT, P-MDT and P-Mg were established to clarify the stress and strain distributions for these specimens upon compression. The material property data of Mg and Ta were obtained from the FEM library. Based on a high computational efficiency and representativeness, the height of the models was reduced by 75% compared with that of the experimental specimens. As shown in Fig. 4a, the stress mainly concentrated in the pore walls of the models when compressing the models of a 5% strain. Especially in the P-MT and P-MDT models, the stress concentration also appeared upon the Ta wires, indicating that the Ta wires served as a stress carrier. It was worth noting that the stress of the Mg matrix in the P-MT model was larger than that in the P-MDT model. Fig. 4b shows the compressive stress-strain curves of the models. The compressive yield strength of the P-MT model was highest, in sequence followed by those of the P-MDT model and the P-Mg model. The strain was further calculated to clarify the effect of the Ta wires on the deformation resistance of the P-MT. The results are depicted in Fig. 4c where the strain evolution of the Mg matrix around the Ta wires was clearly observed. As shown in the square frame of the model, the deformed Mg encountered the hard Ta wires at a strain of 2%. At a strain of 3%, the deformed Mg spread around the Ta wires. At a strain of 4%, the above Mg passed through the Ta wires. The Mg matrix with large deformation was again extended to the Ta wires when the compressive strain increased to 5%. However, there was no apparent deformation upon the Ta wires under the compression, suggesting that the hard Ta wires could effectively hinder the arbitrarily deformation of the Mg matrix.

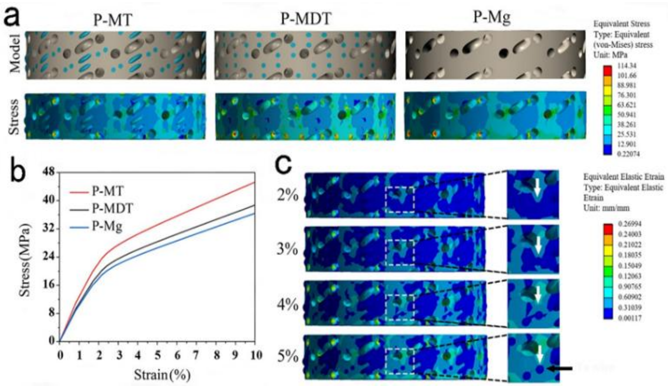

Fig. 4: Finite element analysis of the specimens. (a) Stress distribution of the P-MT, P-MDT and P-Mg models upon compression strain of 5%, (b) The compressive stress-strain curves of the P-MT, P-MDT and P-Mg models with 30% porosity, (c) Strain distribution in the P-MT model with 30% porosity at compressive strains of 2%, 3%, 4%, and 5%.

Fig. 5a exhibits the appearance of the P-MT and P-Mg scaffolds with 30% porosity after the immersion times of 0, 32 h, 64 h, 96 h, 128 h and 160 h. Obviously, in the two cases the Mg matrix gradually degraded with prolonging the immersion time, and accordingly the channel-like holes of the scaffolds enlarged. Particularly, the Ta wires in the P-MT scaffolds were left after the Mg matrix almost degraded. Specifically, after the 160-h immersion, a large amount of Ta wire was clearly distinguished in the P-MT scaffold. The Mg in the P-MT scaffold was completely degraded after the 192-h immersion. The pH value of Hank's solution was related to the degradation rate of Mg matrix. As shown in Fig. 5b, the pH value in the P-MT group was slightly higher than that in the P-Mg group in the immersion period of from 0 to 48 h, while in the period of from 48 to 192 h, it in the former was lower than that in the latter. The hydrogen evolution rate was calculated to further assess the degradation behavior of the scaffolds. As shown in Fig. 5c, the hydrogen evolution rate of the P-MT scaffolds was slightly higher and then lower than that of the P-Mg scaffolds during immersion. This was in consistent with the result of pH analysis.

3.3 In vitro biocompatibility

In vitro assays were conducted to evaluate the cytotoxicity of the P-MT and P-Mg scaffolds compared with the culture medium as a control group. Actin filaments were stained with FITC-Phalloidin to visualize the cytoskeleton of the osteoblasts cultivated in the present of the scaffolds. As seen in Fig. 6a, the cells, adhered to the P-MT and P-Mg scaffolds, were flattened, which had distinct actin filaments, suggesting a good spreadability on the scaffolds. The cytotoxicity of the P-MT scaffolds was assessed by using the live/dead staining method. The cells were cultured in the medium containing the extracts of the scaffolds for 1 and 3 days. As shown in Fig. 6b, most cells of each group were viable during cultivation. The number of the cells increased significantly over the cultivation time. The density of the cells in the P-MT and P-Mg groups was larger than that in the culture medium, suggesting that the P-MT specimens had no obvious cytotoxicity. The cell viability was further evaluated by using MTT assays. As seen in Fig. 6c, the cell viability gradually increased from 1 day to 7 days. The cell viability of the osteoblasts cultivated in the P-MT and P-Mg extracts was higher than that in the culture medium. The cell viability had no significant difference between the P-MT and P-Mg groups. ALP activity was measured to study the effect of the P-MT on the cell differentiation. As shown in Fig. 6d, the cells cultured on both P-MT and P-Mg groups exhibited a high ALP activity compared with the culture medium, indicating that cell differentiation was enhanced in the extracts of the scaffolds.

3.4 In vivo osseointegration

In vitro rabbit experiments aimed at evaluating the osseointegration of the P-MT scaffolds. Fig. 7a exhibits the Micro-CT images of the P-MT, P-Mg and control groups. The scaffolds were implanted in the distal femurs (Zones marked by blue arrows in Fig. 7a). After implantation of 8 weeks, for the control group, little new bone was generated in the defects of rabbit femurs. However, for the P-MT and P-Mg groups, newly formed bone could be identified from the boundary of

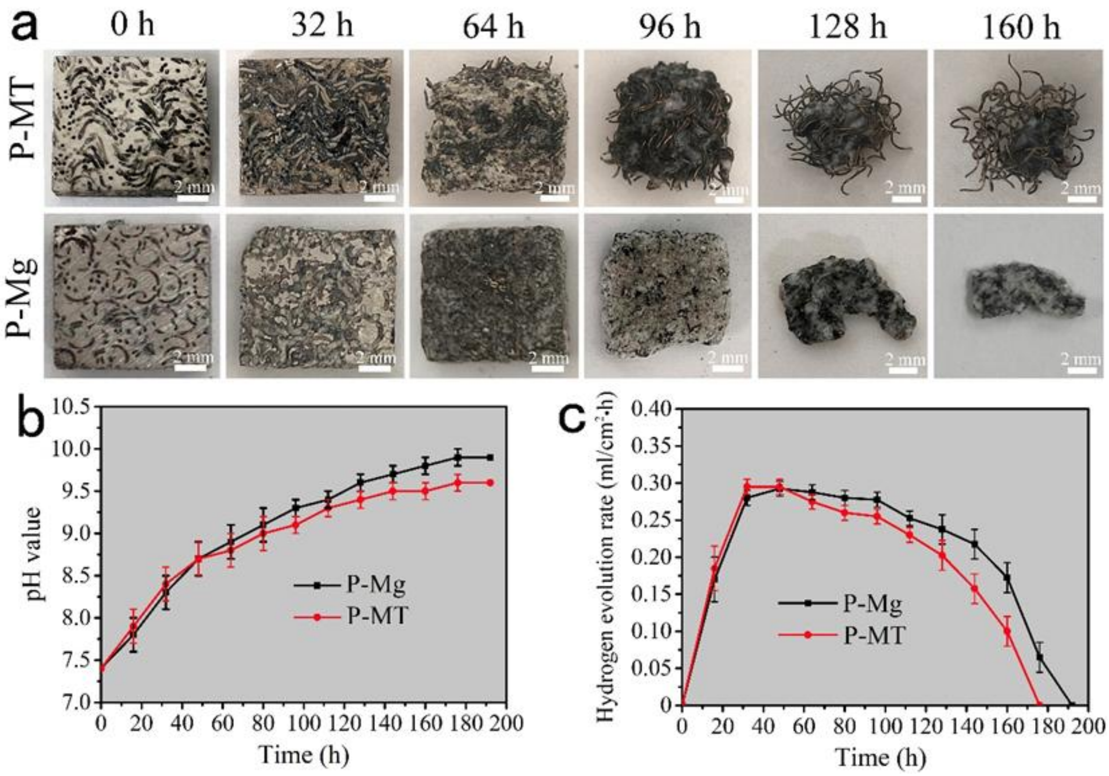

Fig. 5: The degradation behaviors of the P-MT and P-Mg scaffolds with 30% porosity. (a) The appearance of the scaffolds immersed in Hank’s solution for 0 - 192 h, (b) Effect of the immersion time on the pH value of the Hank’s solution, (c) Effect of the immersion time on the Hydrogen evolution rate of the scaffolds in the Hank’s solution.

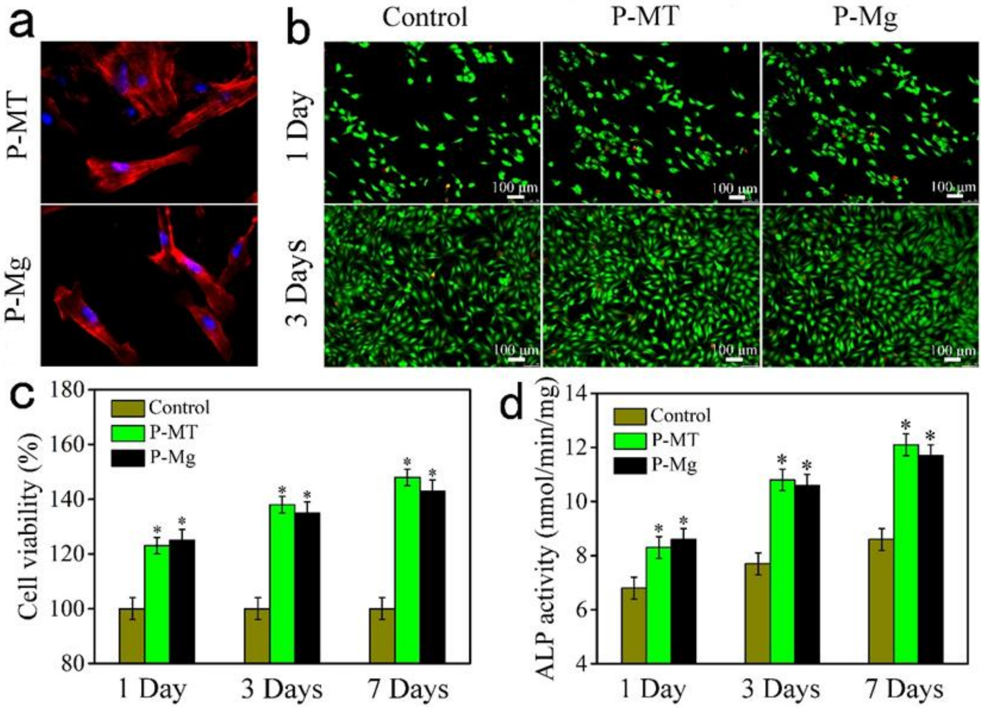

Fig. 6: The biocompatibility of both the P-MT and P-Mg scaffolds with 50% porosity were evaluated. (a) The cytoskeleton of the osteoblasts adhered on scaffolds after 24 h incubation. Actin filaments and cell nuclei were stained with FITC-Phalloidin and DAPI, respectively, (b) Viability of the osteoblasts in the extracts of the P-MT and P-Mg scaffolds was assessed by using live/dead assay, (c) Viability of the osteoblasts in the P-MT and P-Mg groups was evaluated by using MTT assay, (d) ALP activity of the osteoblasts in the P-MT and P-Mg groups (*$p < 0.05$, **$p < 0.01$ vs. Control group).

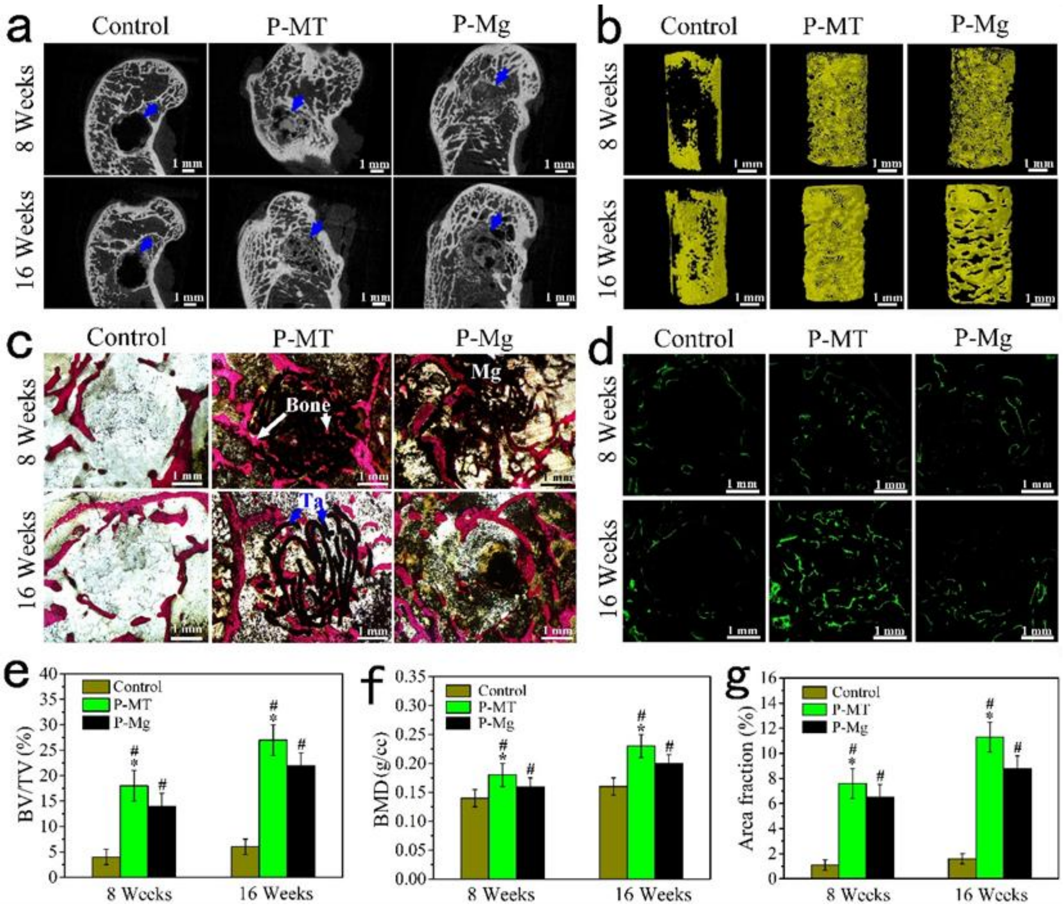

Fig. 7: In vitro rabbit experiments aimed at evaluating the osseointegration of the P-MT scaffolds with 50% porosity. (a) Micro-CT images of the scaffolds and its surrounding femur after implantation of 8 and 16 weeks, respectively, (b) 3D reconstruction models of the scaffolds, in which yellow region represents the bone tissue, (c) Histological observations of the transverse sections of the scaffolds. Undecalcified sections of the scaffolds were stained with acid fuchsin (Red region represented the bone tissue), (d) Sequential polychrome label observation at 8 weeks and 16 weeks: green zones represent the labels stained by calcein at 6 weeks and 12 weeks. Bone volume fraction, BV/TV (e), and bone mineral density, BMD (f), in the scaffolds after implantation of 8 weeks and 16 weeks, (g) The area fraction of new bone tissue stained by the fluorochrome after 8 weeks and 16 weeks post-surgery. $*p < 0.05$ vs. P-Mg, $^{\#}p < 0.05$ vs. Control.

defects when Mg was partially degraded to form discrete large holes in the scaffolds. At 16 weeks post-surgery, the amount of new bone had no significant increased for the control group, while the new bone could be identified around the scaffolds, suggesting that the scaffolds promoted the new bone regeneration. The 3D models of new bone were reconstructed to reveal the osseointegration of the implants, as shown in Fig. 7b. The amount of the new bone in the models increased with the implantation time from 8 weeks to 16 weeks. The surfaces of the cylinder model were covered by little bone for the control group, while the surface of the P-MT and P-Mg models was basically covered by the new bone that permeated into the scaffolds. As shown in Fig. 7c, bone tissue sections were performed to further evaluate the osseointegration of the P-MT scaffolds. Little new bone was formed in the defects of rabbit femurs without the implants at 8 weeks and 16 weeks post-surgery. At 8 weeks post-surgery, the P-MT scaffolds were degraded and remained partial Mg residues in the defects, when a small amount of newly formed bone was identified in the scaffolds. At 16 weeks, the P-MT scaffolds were completely degraded, and no residue was found in the defects. Furthermore, a large amount of new bone was found to form along the retained Ta wires. For the P-Mg scaffolds, new bone was regenerated around the boundary of the scaffolds after implantation of 8 weeks. At 16 weeks post-surgery, the newly formed bone slowly spread from the boundary to the center of the defects. New bone was recorded by the fluorochrome to calculate the bone formation rate, as shown in Fig. 7d. Green regions represent the labels by calcein at 6 weeks and 12 weeks post-surgery. The new bone was sequentially evaluated after implantation 8 weeks and 16 weeks. Few fluorochromes labels were detected in the defects of the femurs at 8 weeks and 16 weeks post-surgery. The density of the green fluorochrome in the P-MT group was larger than that in the P-Mg and control groups, suggesting that the Ta wires stimulated more bone formation in the porous scaffolds.

As depicted in Fig. 7e-f, the quantitative assessment of new bone formation indicated that the BV/TV and BMD gradually increased with the implantation time. The BV/TV in the control group increased from 4% to 6% with the implantation time from 8 weeks to 16 weeks. The BV/TV of 18% in the P-MT group was higher than that of 14% in the P-Mg group at 8 weeks post-surgery. After implantation of 16 weeks, the advantage of the BV/TV in the P-MT group extended to 5% compared with the case of the P-Mg group. Besides, the BMD value in the P-MT was still higher than those in the P-Mg and control group at 8 weeks and 16 weeks post-surgery, indicating that the Ta wires promoted the osseointegration of the P-MT scaffolds in animals. As seen in Fig. 7g, for the control group, the calcein labeling area increased from 1.1% at 8 weeks post-surgery to 1.6% at 16 weeks post-surgery. The calcein labeling area fraction for P-MT group was 7.6% at 8 weeks post-surgery when the calcein labeling area fraction for P-Mg group was 6.5%. At 16 weeks post-surgery, the labeling area fraction for the P-MT group and P-Mg group was 11.3% and 8.8%, respectively. Therefore, the formation rate of new bone in the P-MT group was faster than those in the control and P-Mg groups.

4. Discussion

4.1 Formation mechanism of P-MT

The infiltration casting was an efficient method to prepare the P-MT material. The isodiametric holes were formed after selectively dissolving the circular-section Ti wire from the Mg/Ti/Ta composite. Complete dissolution of the Ti wire in the composite was demonstrated by the weighing method.[27] XRD and EDS results of the cross section of P-MT further suggested that the Ti wire was removed from the composite (Fig. 2f-h). The holes of the P-MT were interconnected because the space holder of the composite was indeed only one single Ti wire. The interconnectivity of these holes was also verified by tomography images in our previous work.[11] The porosity and pore diameter of the P-MT could be controlled by tailoring the volume fraction and diameter of the space holder in the green composite. The surface topographic feature of the Ti wire was reversely replicated by the flow line reliefs on the inner hole surface of the scaffolds in Fig. 2e, which would be beneficial to the cell adhesion and cell proliferation of the porous scaffolds.[31]

Because of the low casting temperature and short holding time, the Ta wire could not react with the Mg matrix during pouring. Thus, the diameter of the Ta wire in the P-MT was identical to that of the original unimplanted one (Fig. 2d). Because the standard electrode potential of Ta (+ 0.67 V) was higher than those of Mg (- 2.37 V) and Ti (- 1.63 V), the Ta wires in the composite were not corroded by the HF solution during the electrochemical process. Li *et al.* studied the corrosion behavior of the Ta in the HF solution, and found that a compact passivation film comprising of Ta_2O_5, formed on the Ta metal surface, could prevent the permeation of F ions, thus promoting corrosion resistance.[32] On the other hand, Mg was also passivated in the HF solution to form a MgF_2 layer, which could prevent further reactions of the metal Mg and HF solution.[33] However, a severe attack on Ti metal was induced by fluoride ions in an acidic solution, in which Ti formed the ions $[TiF_6]^{2-}$.[34] The electrochemical reaction would continually proceed until the Ti wire was completely dissolved from the composite. The differentiated response between Mg and Ti in the HF solution had been discussed in detail in the previous report.[9] Therefore, only the Ti wire was selectively corroded from the Mg/Ti/Ta composite.

4.2 Influences of the Ta wires on the compressive and degradation properties of P-MT

The stress-strain curves of the P-MT specimens were smooth during quasi-static compression (Fig. 3c), indicating that the specimens underwent bulk deformation rather than local collapse. The compressive load could be effectively transferred from the Mg matrix to the Ta wires, because there was no gap between the two parts (Fig. 2d). Besides, Ta has a higher compressive strength than pure Mg.[35,36] Therefore, the Ta wires in the P-MT model exhibited a high stress value compared to its surrounding Mg matrix, as shown in Fig. 4a. Compared with the P-Mg with 50% porosity, the compressive yield strength and modulus of the P-MT with 50% porosity grew 93% and 88%, respectively. Indeed, the effect of the Ta wires on the P-MT could be also observed from the stress-strain curves of the simulation models (Fig. 4). As seen in Fig. 8a, the compressive yield strength of the P-MDT model was 27.5 MPa, which was higher than 23.7 MPa of the P-Mg model, and lower than 33.8 MPa of the P-MT model. Fig. 8b-c concluded the strengthening mechanism of the Ta wires on the P-Mg. On the one hand, the continuous Ta wires would be reserved during the immersion, which continued to provide a support for the P-MT scaffolds. However, the supporting effect of the Ta wires for the P-MT would disappear when the Ta wires were truncated, as shown in Fig. 8b. On the other hand, the continuity of the deformation in the P-MT was broken as the deformation path of Mg was hindered by the high-strength Ta wires. The deformed Mg gradually

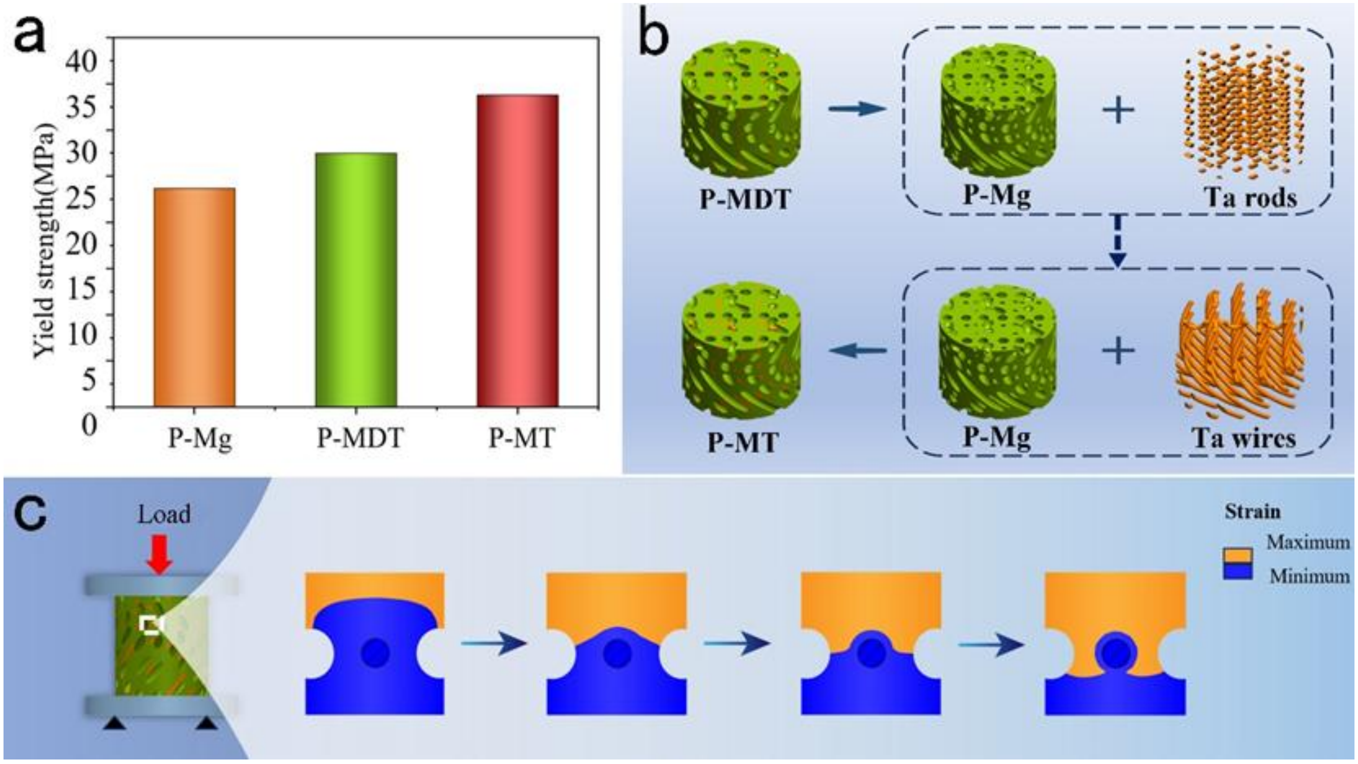

Fig. 8: The strengthening mechanism of the Ta wires on the P-MT. (a) The compressive yield strength of the P-Mg, P-MDT and P-MT models with 30% porosity, (b) The Ta wires also played a support role for the P-MT when the Ta rods in the P-MDT were replaced by the Ta wires, (c) The hindering effect of the Ta wires on the Mg matrix during the deformation process of the P-MT.

accumulated around the Ta wires. As the strain reached a limit, the deformed Mg could bypass the Ta wires. The high-strength Ta wire increased the deformation resistance of the P-MT, enhancing its compressive strength, as shown in Fig. 8c. This strengthening mechanism is similar to a role of hard phase in the second phase strengthening.[37] Therefore, the Ta wires had dual strengthening effects on the P-MT. A previously reported 3D-printed P-Mg material with 50% porosity had a compressive yield strength of 8.7 MPa.[38] This value is higher than that of our P-Mg (5.6 MPa) but lower than that of our P-MT (10.8 MPa), demonstrating the superior mechanical properties of the P-MT scaffold.

Porosity had a significant effect on the compressive properties of the porous materials.[39] As shown in Fig. 2a, the holes, regarded as the defects during compression, uniformly distributed on the section of the P-MT specimens. The number of the holes of the specimens at a high porosity was more than that at a low porosity. Besides, the specimens at the high porosity had a small average CWT and then weak deformation resistance. Thus, the compressive yield strength of the P-MT specimens gradually decreased with increasing the porosity. Because a high porosity was beneficial to the bone ingrowth into the implants in the range of 30%-80%,[40] the specimen with 50% porosity in the investigated specimens was chosen to evaluate the osseointegration of the P-MT. The yield strength and elastic modulus of the P-MT with 50% porosity were comparable to those of cancellous bone (yield strength of 3-20 MPa,[41] and modulus of 0.1-3.0 GPa[42]), effectively preventing the premature failure of the P-MT scaffolds.

The compressive property of the Mg scaffolds in body fluids constantly deteriorated because of the Mg degradation.[43] A large degradation rate would result in a rapid decrease in the compressive strength of scaffolds. After the 48-h immersion in Hank's solution, the degradation rate of the P-MT scaffolds increased approximately 5% compared to that of the P-Mg scaffolds, as shown in Fig. 5b-c. An electrochemical reaction between Ta and Mg would occur in the electrolyte solution.[44] Because the standard electrode potential of Ta was higher than that of Mg, the Ta served as the cathode while the Mg was the anode in the electrochemical reaction. Therefore, the embedded Ta wires could accelerate the degradation of the Mg scaffolds in Hank's solution. It was worth noting that the degradation rate in the P-MT group was lower than that in the P-Mg group after the immersion time from 48 h to 192 h (Fig. 5), because the mass of Mg in the P-MT group was less than that in the P-Mg group under the same volume.

4.3 Mechanism of the osseointegration improvement by incorporating Ta wires

Osseointegration of the P-MT scaffold was assessed in vitro and in vivo rabbit experiments. The cytoskeletons of osteoblasts cultured in the extracts of the P-MT scaffolds were clearly visible. The density of the living cells between the P-MT and control group was basically identical, indicating that there was no indirect cytotoxicity in the P-MT scaffolds prepared by infiltration casting technology. A large amount of extract could be collected from the culture medium after the Mg matrix was degraded. Han *et al.* had validated that the extract from Mg screws could promote the cell differentiation of the scaffolds.[45] The extracts from the P-MT and P-Mg scaffolds promoted the level of ALP ability (Fig. 6d). Although cell viability and differentiation of osteoblasts cultured in the P-MT group were great compared to the culture medium, it had no apparent difference between the P-MT and P-Mg groups.

The porous scaffolds could facilitate vascularization in the defects of hosts, which reduced risk of nonunion and healing time.[46] Therefore, the P-MT and P-Mg groups had a better osseointegration compared to the control group. The entangled Ta wires in the P-MT were still reserved when the Mg matrix was completely degraded at 16 weeks post-surgery. Indeed, Ta had been widely used as an orthopedic implant material.[17,25] In vivo tests demonstrated that the Ta implant has a good biocompatibility and osseointegration.[47] In this study, the Ta wires exhibited no cytotoxicity (Fig. 6), and excellent osteogenesis (Fig. 7), indicating that it was safe as a reinforced fiber to be embedded in the scaffolds. It was worth noting that the entangled Ta wires had a similar spatial structure to bone trabecula. Wang *et al.* studied the biological properties of the entangled metal wire by in vivo experiments, and found that the entangled porous structure could promote osseointegration of the scaffolds.[48] As seen in Fig. 7c, the new bone was preferentially generated on the entangled Ta wires at post-surgery. Therefore, the P-MT scaffolds had a superior osseointegration compared with the P-Mg scaffolds.

Fig. 9 concluded the influence mechanism of the Ta wires on the osseointegration of the P-MT scaffolds. After the scaffolds were implanted into the rabbit femur defects, the new bone was gradually regenerated in the holes of the porous scaffolds. The Ta wires of the P-MT scaffolds were reserved when the Mg matrix was gradually degraded during the implantation. The Ta wires provided stable attachment points for the new bone formation after the Mg matrix was degraded. It was worth noting that there were no Mg residues in the defect at 16 weeks post-surgery (Fig. 7b), suggesting that the scaffolds had lost most of the mechanical property. However, the mechanical support of 12-24 weeks should be provided by the scaffolds based on the clinical conditions.[49] Therefore,

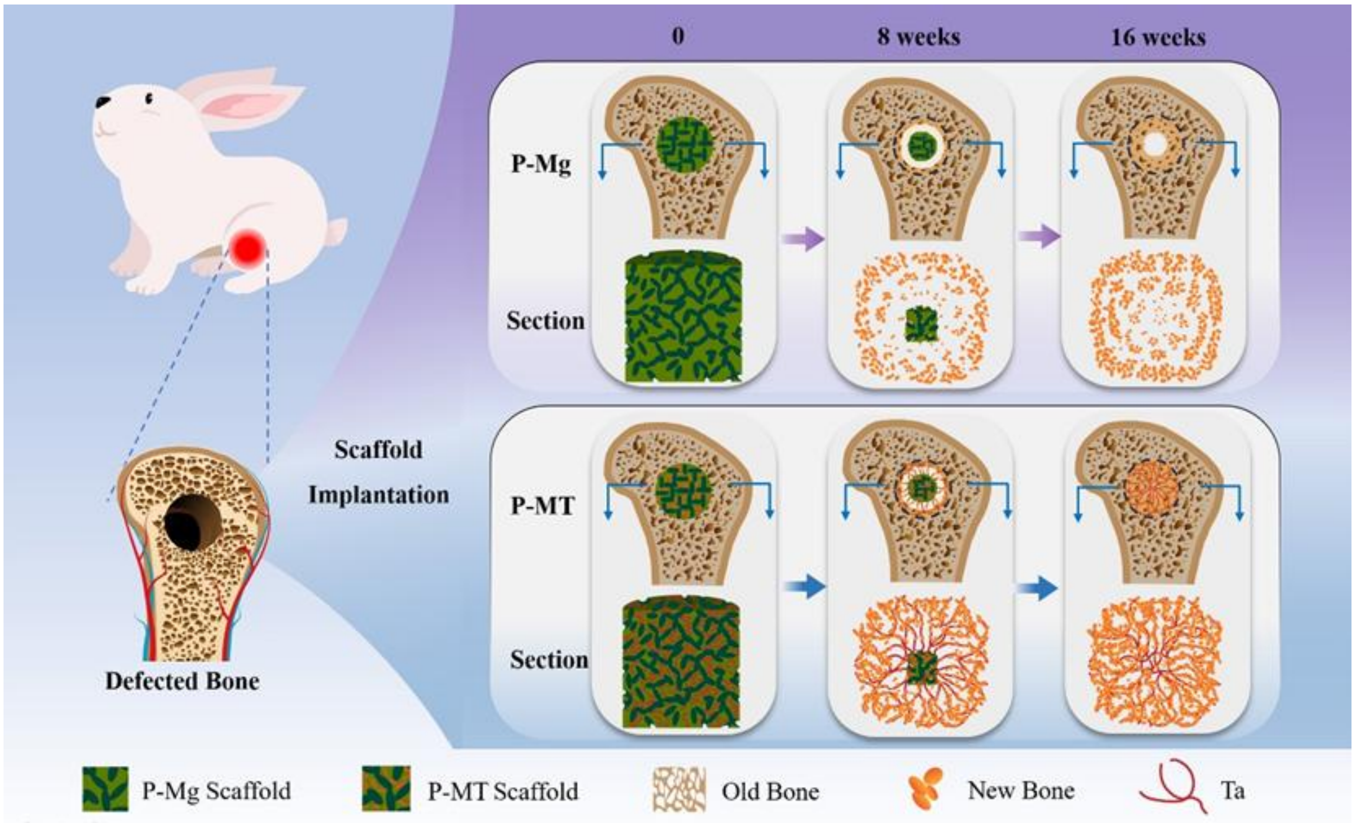

Fig. 9: Illustration of influencing mechanisms of the Ta wires on the osseointegration of the P-MT scaffolds.

it was important for the P-MT scaffolds to meet the degradation requirement. In the future, the surface modification, such as micro arc oxidation and anodization,[50] would be introduced to control the degradation rate of the P-MT scaffolds.

5. Conclusion

In this study, the P-MT scaffolds were successfully prepared by the infiltration casting technology. The mechanical property was studied by the quasi-static compression tests, and the osseointegration was investigated by in vitro and in vivo rabbit femur experiments. The FE models were established to simulate the stress and strain distribution of the specimens. The main conclusions were as follow.

(1) The P-MT was composed of Mg matrix, holes and Ta wires, in which the Ta wires were embedded in the Mg matrix. The holes were isodiametric and interconnected. The porosity and pore size of the P-MT could be controlled by using different space holder. The average CWT of the P-MT decreased from 308.2 μm to 241.4 μm with increasing porosity from 30% to 50%.

(2) The Ta wires had an important effect on the compressive and degradation properties of the P-MT. When compressing the P-MT, the high-strength Ta wires increased the resistance to deformation, and provided a supporting effect. The compressive yield strength and modulus of the P-MT with 50 % porosity were 10.8 MPa and 1.5 GPa, which grew 93% and 88% compared to the P-Mg, respectively. The compressive properties of the P-MT were comparable to cancellous bone. The degradation rate of the P-MT was slightly higher and then lower than that of the P-Mg.

(3) There was no obvious cytotoxicity in the P-MT scaffolds. The Ta wire provided a convenient attachment point for the new bone growth into the P-MT scaffolds. The BV/TV and BMD of the P-MT scaffolds were higher than that of the P-Mg scaffolds, indicating that the P-MT had a better osseointegration than the P-Mg. The P-MT material has a promising application on the bone defects repair.

Acknowledgments

The fund of Henan Key Laboratory of Superhard Abrasives and Grinding Equipment, Henan University of Technology (No. JDKFJJ2024008), Natural Science Foundation of Henan (No. 242300420024), and Key Research Project Plan for Higher Education Institutions in Henan Province (No. 26A430006).

Conflict of Interest

The authors declare that they have no known competing financial interests or personal relationships that could have appeared to influence the work reported in this paper.

Supporting Information

Not applicable.

CRediT Statement

D. Wang: assisted by **L. Wu:** Conceived the concept, Wrote the original draft and acquired funds. **J. Li and Y.G. Guo:** performed the experiments and analyzed the data. **Y. Chang**: Designed the methodology and operated the software. **Z. Chai:** Reviewed and edited the manuscript. **X.L. Zhang:** Performed the biological experiments and formal analysis. All authors reviewed and edited the final version of the manuscript.

References

[1] J.-L. Wang, J.-K. Xu, C. Hopkins, D. H. Chow, L. Qin, Biodegradable magnesium-based implants in orthopedics: a general review and perspectives, *Advanced Science*, 2020, **7**, 1902443, doi: 10.1002/advs.201902443.

[2] N. Sezer, Z. Evis, M. Koç, Additive manufacturing of biodegradable magnesium implants and scaffolds: Review of the recent advances and research trends, *Journal of Magnesium and Alloys*, 2021, **9**, 392-415, doi: 10.1016/j.jma.2020.09.014.

[3] M. Nasr Azadani, A. Zahedi, O. K. Bowoto, B. I. Oladapo, A review of current challenges and prospects of magnesium and its alloy for bone implant applications, *Progress in Biomaterials*, 2022, **11**, 1-26, doi: 10.1007/s40204-022-00182-x.

[4] Y. Li, J. Zhou, P. Pavanram, M. A. Leeflang, L. I. Fockaert, B. Pouran, N. Tümer, K. U. Schröder, J. M. C. Mol, H. Weinans, H. Jahr, A. A. Zadpoor, Additively manufactured biodegradable porous magnesium, *Acta Biomaterialia*, 2018, **67**, 378-392, doi: 10.1016/j.actbio.2017.12.008.

[5] X. N. Gu, W. R. Zhou, Y. F. Zheng, Y. Liu, Y. X. Li, Degradation and cytotoxicity of lotus-type porous pure magnesium as potential tissue engineering scaffold material, *Materials Letters*, 2010, **64**, 1871-1874, doi: 10.1016/j.matlet.2010.06.015.

[6] N. T. Kirkland, I. Kolbeinsson, T. Woodfield, G. J. Dias, M. P. Staiger, Synthesis and properties of topologically ordered porous magnesium, *Materials Science and Engineering: B*, 2011, **176**, 1666-1672, doi: 10.1016/j.mseb.2011.04.006.

[7] Z. S. Seyedraoufi, S. Mirdamadi, Synthesis, microstructure and mechanical properties of porous Mg–Zn scaffolds, *Journal of the Mechanical Behavior of Biomedical Materials*, 2013, **21**, 1-8, doi: 10.1016/j.jmbbm.2013.01.023.

[8] X. Yue, J. Shang, M. Zhang, B. Hur, X. Ma, Additive manufacturing of high porosity magnesium scaffolds with lattice structure and random structure, *Materials Science and Engineering: A*, 2022, **859**, 144167, doi:

10.1016/j.msea.2022.144167.

[9] G. Jiang, G. He, A new approach to the fabrication of porous magnesium with well-controlled 3D pore structure for orthopedic applications, *Materials Science & Engineering. C, Materials for Biological Applications*, 2014, **43**, 317-320, doi: 10.1016/j.msec.2014.07.033.

[10] Q. Li, G. Jiang, J. Dong, J. Hou, G. He, Damping behavior and energy absorption capability of porous magnesium, *Journal of Alloys and Compounds*, 2016, **680**, 522-530, doi: 10.1016/j.jallcom.2016.04.101.

[11] D. Wang, G. He, Y. Tian, N. Ren, J. Ni, W. Liu, X. Zhang, Evaluation of channel-like porous-structured titanium in mechanical properties and osseointegration, *Journal of Materials Science & Technology*, 2020, **44**, 160-170, doi: 10.1016/j.jmst.2019.10.026.

[12] R. Bonithon, C. Lupton, M. Roldo, J. N. Dunlop, G. W. Blunn, F. Witte, G. Tozzi, Open-porous magnesium-based scaffolds withstand *in vitro* corrosion under cyclic loading: a mechanistic study, *Bioactive Materials*, 2023, **19**, 406-417, doi: 10.1016/j.bioactmat.2022.04.012.

[13] T. Kim, C. W. See, X. Li, D. Zhu, Orthopedic implants and devices for bone fractures and defects: Past, present and perspective, *Engineered Regeneration*, 2020, **1**, 6-18, doi: 10.1016/j.engreg.2020.05.003.

[14] N. Zou, Q. Li, Mechanical properties of lightweight porous magnesium processed through powder metallurgy, *JOM*, 2018, **70**, 650-655, doi: 10.1007/s11837-018-2772-9.

[15] N. Zou, Q. Li, Compressive mechanical property of porous magnesium composites reinforced by carbon nanotubes, *Journal of Materials Science*, 2016, **51**, 5232-5239, doi: 10.1007/s10853-016-9824-8.

[16] M. Liu, Z. Li, F. Li, Q. Jin, X. Yang, C. Xia, Mechanical properties and *in vitro* biodegradation behavior of GASAR porous Mg-Ag alloy, *Materials Letters*, 2022, **315**, 131920, doi: 10.1016/j.matlet.2022.131920.

[17] S. T. Rajan, M. Das, A. Arockiarajan, *In vitro* biocompatibility and degradation assessment of tantalum oxide coated Mg alloy as biodegradable implants, *Journal of Alloys and Compounds*, 2022, **905**, 164272, doi: 10.1016/j.jallcom.2022.164272.

[18] J. Yang, X. Jin, H. Gao, D. Zhang, H. Chen, S. Zhang, X. Li, Additive manufacturing of trabecular tantalum scaffolds by laser powder bed fusion: Mechanical property evaluation and porous structure characterization, *Materials Characterization*, 2020, **170**, 110694, doi: 10.1016/j.matchar.2020.110694.

[19] M. P. Staiger, A. M. Pietak, J. Huadmai, G. Dias, Magnesium and its alloys as orthopedic biomaterials: a review, *Biomaterials*, 2006, **27**, 1728-1734, doi: 10.1016/j.biomaterials.2005.10.003.

[20] A. Vahid, P. Hodgson, Y. Li, New porous Mg composites for bone implants, *Journal of Alloys and Compounds*, 2017, **724**, 176-186, doi: 10.1016/j.jallcom.2017.07.004.

[21] Z. Shan, X. Xie, X. Wu, S. Zhuang, C. Zhang, Development of degradable magnesium-based metal implants and their function in promoting bone metabolism (a review), *Journal of Orthopaedic Translation*, 2022, **36**, 184-193, doi: 10.1016/j.jot.2022.09.013.

[22] J. A. Kim, J. Lim, R. Naren, H. S. Yun, E. K. Park, Effect of the biodegradation rate controlled by pore structures in magnesium phosphate ceramic scaffolds on bone tissue regeneration in vivo, *Acta Biomaterialia*, 2016, **44**, 155-167, doi: 10.1016/j.actbio.2016.08.039.

[23] Q. Dong, Y. Li, H. Jiang, X. Zhou, H. Liu, M. Lu, C. Chu, F. Xue, J. Bai, 3D-cubic interconnected porous Mg-based scaffolds for bone repair, *Journal of Magnesium and Alloys*, 2021, **9**, 1329-1338, doi: 10.1016/j.jma.2020.05.022.

[24] H. Xu, Q. Li, Deformation mechanisms and mechanical properties of porous magnesium/carbon nanofiber composites with different porosities, *Journal of Materials Science*, 2018, **53**, 14375-14385, doi: 10.1007/s10853-018-2649-x.

[25] Y. Guo, K. Xie, W. Jiang, L. Wang, G. Li, S. Zhao, W. Wu, Y. Hao, *In vitro* and *in vivo* study of 3D-printed porous tantalum scaffolds for repairing bone defects, *ACS Biomaterials Science & Engineering*, 2019, **5**(2), 1123-1133, doi: 10.1021/acsbiomaterials.8b01094.

[26] Y. Guo, C. Chen, Q. Wang, Y. Cao, C. Wu, K. Zhou, Microstructural evolution and mechanical behavior of additively manufactured tantalum produced by electron beam powder bed fusion, *International Journal of Refractory Metals and Hard Materials*, 2023, **110**, 106046, doi: 10.1016/j.ijrmhm.2022.106046.

[27] D. Wang, Q. Li, M. Xu, G. Jiang, Y. Zhang, G. He, A novel approach to fabrication of three-dimensional porous titanium with controllable structure, *Materials Science and Engineering: C*, 2017, **71**, 1046-1051, doi: 10.1016/j.msec.2016.11.119.

[28] Q. Li, Y. Zhang, D. Wang, H. Wang, G. He, Porous polyether ether ketone: a candidate for hard tissue implant materials, *Materials & Design*, 2017, **116**, 171-175, doi: 10.1016/j.matdes.2016.12.012.

[29] S. R. Kalidindi, A. Abusafieh, E. El-Danaf, Accurate characterization of machine compliance for simple compression testing, *Experimental Mechanics*, 1997, **37**, 210-215, doi: 10.1007/BF02317861.

[30] M.-Q. Cheng, T. Wahafu, G.-F. Jiang, W. Liu, Y.-Q. Qiao, X.-C. Peng, T. Cheng, X.-L. Zhang, G. He, X.-Y. Liu, A novel open-porous magnesium scaffold with controllable microstructures and properties for bone regeneration, *Scientific Reports*, 2016, **6**, 24134, doi: 10.1038/srep24134.

[31] D. Wang, G. He, Y. Tian, N. Ren, W. Liu, X. Zhang, Dual effects of acid etching on cell responses and mechanical properties of porous titanium with controllable open-porous structure, *Journal of Biomedical Materials Research Part B: Applied Biomaterials*, 2020, **108**, 2386-2395, doi: 10.1002/jbm.b.34571.

[32] I. Suni, Electrochemistry of Ta in aqueous HF, *ECS Transactions*, 2007, **2**, 439-444, doi: 10.1149/1.2408897.

[33] J. E. Gray, B. Luan, Protective coatings on magnesium and its alloys: a critical review, *Journal of Alloys and Compounds*, 2002, **336**, 88-113, doi: 10.1016/S0925-8388(01)01899-0.

[34] F. Toumelin-Chemla, F. Rouelle, G. Burdairon, Corrosive properties of fluoride-containing odontologic gels against

titanium, *Journal of Dentistry*, 1996, **24**, 109-115, doi: 10.1016/0300-5712(95)00033-X.

[35] M. El-Tahawy, P. Jenei, T. Kolonits, G. Han, H. Park, H. Choe, J. Gubicza, Different evolutions of the microstructure, texture, and mechanical performance during tension and compression of 316L stainless steel, *Metallurgical and Materials Transactions A*, 2020, **51**, 3447-3460, doi: 10.1007/s11661-020-05782-5.

[36] W. Lei, H. Zhang, Analysis of microstructural evolution and compressive properties for pure Mg after room-temperature ECAP, *Materials Letters*, 2020, **271**, 127781, doi: 10.1016/j.matlet.2020.127781.

[37] W. Zhang, Z. Ma, H. Zhao, L. Ren, Refinement strengthening, second phase strengthening and spinodal microstructure-induced strength-ductility trade-off in a high-entropy alloy, *Materials Science and Engineering: A*, 2022, **847**, 143343, doi: 10.1016/j.msea.2022.143343.

[38] X. Zhang, X.-W. Li, J.-G. Li, X.-D. Sun, Preparation and mechanical property of a novel 3D porous magnesium scaffold for bone tissue engineering, *Materials Science and Engineering: C*, 2014, **42**, 362-367, doi: 10.1016/j.msec.2014.05.044.

[39] X. C. Xia, X. W. Chen, Z. Zhang, X. Chen, W. M. Zhao, B. Liao, B. Hur, Effects of porosity and pore size on the compressive properties of closed-cell Mg alloy foam, *Journal of Magnesium and Alloys*, 2013, **1**, 330-335, doi: 10.1016/j.jma.2013.11.006.

[40] A. Bansiddhi, T. D. Sargeant, S. I. Stupp, D. C. Dunand, Porous NiTi for bone implants: a review, *Acta Biomaterialia*, 2008, **4**, 773-782, doi: 10.1016/j.actbio.2008.02.009.

[41] A.F. Tencer, K.D. Johnson, Biomechanics in Orthopedic Trauma: Bone Fracture and Fixation, CRC Press, London, 1994, ISBN: 1853171085.

[42] M. Geetha, A. K. Singh, R. Asokamani, A. K. Gogia, Ti based biomaterials, the ultimate choice for orthopaedic implants–A review, *Progress in Materials Science*, 2009, **54**, 397-425, doi: 10.1016/j.pmatsci.2008.06.004.

[43] Q. Dong, Y. Li, H. Jiang, X. Zhou, H. Liu, M. Lu, C. Chu, F. Xue, J. Bai, 3D-cubic interconnected porous Mg-based scaffolds for bone repair, *Journal of Magnesium and Alloys*, 2021, **9**, 1329-1338, doi: 10.1016/j.jma.2020.05.022.

[44] J. Xu, D. Wu, B. Ge, M. Li, H. Yu, F. Cao, W. Wang, Q. Zhang, P. Yi, H. Wang, L. Song, L. Liu, J. Li, D. Zhao, Selective laser melting of the porous Ta scaffold with Mg-doped calcium phosphate coating for orthopedic applications, *ACS Biomaterials Science & Engineering*, 2024, **10**, 1435-1447, doi: 10.1021/acsbiomaterials.3c01503.

[45] P. Han, P. Cheng, S. Zhang, C. Zhao, J. Ni, Y. Zhang, W. Zhong, P. Hou, X. Zhang, Y. Zheng, Y. Chai, *In vitro* and *in vivo* studies on the degradation of high-purity Mg (99.99wt.%) screw with femoral intracondylar fractured rabbit model, *Biomaterials*, 2015, **64**, 57-69, doi: 10.1016/j.biomaterials.2015.06.031.

[46] E. Roddy, M. R. DeBaun, A. Daoud-Gray, Y. P. Yang, M. J. Gardner, Treatment of critical-sized bone defects: clinical and tissue engineering perspectives, *European Journal of Orthopaedic Surgery & Traumatology*, 2018, **28**, 351-362, doi: 10.1007/s00590-017-2063-0.

[47] H. Kenar, E. Akman, E. Kacar, A. Demir, H. Park, H. Abdul-Khaliq, C. Aktas, E. Karaoz, Femtosecond laser treatment of 316L improves its surface nanoroughness and carbon content and promotes osseointegration: an *in vitro* evaluation, *Colloids and Surfaces B: Biointerfaces*, 2013, **108**, 305-312, doi: 10.1016/j.colsurfb.2013.02.039.

[48] Q. Wang, Y. Qiao, M. Cheng, G. Jiang, G. He, Y. Chen, X. Zhang, X. Liu, Tantalum implanted entangled porous titanium promotes surface osseointegration and bone ingrowth, *Scientific Reports*, 2016, **6**, 26248, doi: 10.1038/srep26248.

[49] Y. F. Zheng, X. N. Gu, F. Witte, Biodegradable metals, *Materials Science and Engineering: R: Reports*, 2014, **77**, 1-34, doi: 10.1016/j.mser.2014.01.001.

[50] G. Zhu, G. Wang, J. J. Li, Advances in implant surface modifications to improve osseointegration, *Materials Advances*, 2021, **21**, 6901-6927, doi: 10.1039/D1MA00675D.

Open Access